Journal of
Ship&Ocean
Technology
©MARCH 2004

SOTECH Vol. 8, No. 1, pp. 10 ~ 30, 2004

RANS Simulation of a Tip-Leakage Vortex on a Ducted Marine Propulsor

Jin Kim[1], Eric Peterson[2] and Frederick Stern[3]
[1] Korea Research Institute of Ships & Ocean Engineering, KORDI, Daejeon, Korea;
E-mail: jkkim@kriso.re.kr
[2] Applied Research Laboratory, The Pennsylvania State University, PA, USA
[3] Iowa Institute of Hydraulic Research, The University of Iowa, IA, USA

Abstract

High-fidelity RANS simulations are presented for a ducted marine propulsor, including verification & validation (V&V) using available experimental fluid dynamics (EFD) data. CFDSHIP-IOWA is used with k-ω turbulence model and extensions for relative rotating coordinate system and Chimera overset grids. The mesh interpolation code PEGASUS is used for the exchange of the flow information between the overset grids. Intervals V&V for thrust, torque, and profile averaged radial velocity just downstream of rotor tip are reasonable in comparison with previous results. Flow pattern displays interaction and merging of tip-leakage and trailing edge vortices. In interaction region, multiple peaks and vorticity are smaller, whereas in merging region, better agreement with EFD. Tip-leakage vortex core position, size, circulation, and cavitation patterns for σ=5 also show a good agreement with EFD, although vortex core size is larger and circulation in interaction region is smaller.

Keywords: ducted marine propulsor, high-fidelity RANS, tip-leakage vortex

1 Introduction

The performance of a ducted marine propulsor is influenced by a number of parameters, including tip geometry and gap, blade loading, and boundary layer inflow. Cavitation inception occurs in the tip-leakage vortex core downstream of the rotor trailing edge. Since small bubbles, or nuclei, respond to the local pressure field as they convect through the propulsor, prediction of cavitation inception requires high fidelity resolution of the pressure and associated flow features such as tip-leakage and trailing edge vortices, blade and duct boundary layers, and turbulence. Recent experiments related to tip-leakage vortex for David Taylor Model Basin(DTMB) ducted marine propulor 5206 (Judge et al, 2001) have quantified for the important flow physics.

The design of marine propulsor has been largely based on potential flow theory in combination with experimental testing. While potential flow theory offers a quick way to obtain insight into the global performance characteristics of a propeller such as thrust and torque, it has substantial shortcomings resulting from the assumption of inviscid flow. Important effects like boundary layer separation due to pressure gradients at off design conditions cannot be included in this method. Empirical assumptions about the drag have

to be introduced in order to include some of the effects of viscosity. However, the influence of other viscous effect and turbulence on the performance cannot be modeled in the inviscid methods.

As a result, RANS simulation of a marine propulsor is receiving increased attention. RANS computations for marine propellers with practical geometry have been reported (Sanchez-Caja, 1996; Abdel-Maksoud et al, 1998). The detailed flow at the tip vortex and prediction of trends for various tip-geometries is shown (Hsiao and Pauley, 1998; Feng et al, 1998; Chen, 2000) and the capability of RANS to predict 4-quadrant performance (i.e. ahead, backing, crash-ahead and crash-back) has been studied including detailed analysis of the resulting flow field (Chen and Stern, 1998). All these RANS simulations are performed on open water propellers and used structured grid systems. Each group showed reasonably good agreement with the experimental measurements. The reason for discrepancies between experiment and computation are typically cited to be low grid resolution and over-predicting the eddy viscosity in the vortex core. Recently, Brewer (2002) shows a RANS solution of the ducted marine propulsor 5206. He used an unstructured, unsteady RANS code named U^{2}NCLE with the one-equation turbulence model and approximately 3.5 million nodes for whole 3 blades (360 degree) computational domain.

The objective of the current study is high fidelity RANS simulations for the ducted marine propulsor 5206, including verification studies based on assessment iterative and grid convergence, validation studies using available benchmark experimental fluid dynamics (EFD) data and uncertainties.

2 Computational methods

The three-dimensional incompressible RANS code, CFDSHIP-IOWA (Paterson et al, 2003) is used in the current study. This code has been verified and validated for a range of applications to ship hydrodynamics (Wilson et al, 2000 & 2001). The main change compared with the previous version is the ability to handle the general overset CHIMERA grid and the Cartesian relative rotating frame formulation for marine propulsor application.

2.1 Governing equations for propulsor flow

The unsteady three-dimensional RANS and continuity equations for the incompressible fluid are written in non-dimensional form:

$$\frac{\partial U_i}{\partial x_i} = 0 \tag{1}$$

$$\frac{\partial U_i}{\partial t} + U_j \frac{\partial U_i}{\partial x_j} = -\frac{\partial \hat{p}}{\partial x_i} + \frac{1}{\mathrm{Re}} \frac{\partial^2 U_i}{\partial x_j \partial x_j} - \frac{\partial}{\partial x_j} \overline{u_i u_j} \tag{2}$$

where $U_i = (U, V, W)$ are the Reynolds-averaged velocity components, $x_i = (x, y, z)$ are the Cartesian coordinate systems, $\hat{p} = (p - p_o)/\rho U_0^2$ is the piezometric pressure, $\overline{u_i u_j}$ are the Reynolds stresses, which are one point cross or self correlation of the turbulent fluctuations u_i, and $\mathrm{Re} = U_o D/\nu$ is the Reynolds number. All equations are non-dimensionalized by

the reference velocity U_o, characteristic length D (usually the propeller diameter), reference pressure p_o, and density ρ.

For the marine propulsor flow, the current study adopts the relative frame formulations. Currently, relative-frame motion in Cartesian coordinates is restricted to steady rotation about the x-axis, which is the axis of propeller rotation. For these simple cases, the acceleration term on the left hand side of the equation (2) is replaced with the following expression.

$$\frac{D\mathbf{U}}{Dt} = \frac{D\mathbf{U}'}{Dt} + \begin{pmatrix} 0 \\ -\omega_x^2 y' - 2\omega_x W' \\ -\omega_x^2 z' + 2\omega_x V' \end{pmatrix} \tag{3}$$

where (x', y', z') and (U', V', W') are the coordinates and velocity components in the relative frame. In addition to modifying the acceleration terms, the initial and boundary conditions must be transformed into the relative frame. This results in a large solid-body rotation of the free-stream velocity. Although this is the usual approach to formulating relative-frame codes, an alternative approach is used here which has the benefits of removing the solid-body rotation, moving most of the non-inertial terms from the source-term on the RHS to the convective terms on the LHS of (2), and simplifying calculation of vorticity and wall-shear stress, such that the same algorithms may be used for either reference frame.

To derive such a system of equations, the velocity vectors in the noninertial coordinate can be split with the relative velocity vector and the rotational velocity of the domain. In Cartesian coordinates

$$\begin{pmatrix} U' \\ V' \\ W' \end{pmatrix} = \begin{pmatrix} U'' \\ V'' \\ W'' \end{pmatrix} - \mathbf{\Omega} \times \mathbf{r} = \begin{pmatrix} U'' \\ V'' \\ W'' \end{pmatrix} - \begin{pmatrix} 0 \\ -\omega_x z \\ \omega_x y \end{pmatrix} \tag{4}$$

Substituting Eg. (4) into (1), (2) and (3), and collecting terms provides RANS equations in terms of (U'', V'', W'')

$$\frac{\partial U''}{\partial x} + \frac{\partial V''}{\partial y} + \frac{\partial W''}{\partial z} = 0 \tag{5}$$

$$\frac{\partial U''}{\partial t} + U''\frac{\partial U''}{\partial x'} + (V'' + \omega_x z')\frac{\partial U''}{\partial y'} + (W'' - \omega_x y')\frac{\partial U''}{\partial z'} = -\frac{\partial \hat{p}}{\partial x'} + \frac{1}{Re}\frac{\partial^2 U''}{\partial x_j \partial x_j} - \frac{\partial}{\partial x_j'}\overline{uu_j} \tag{6}$$

$$\frac{\partial V''}{\partial t} + U''\frac{\partial V''}{\partial x'} + (V'' + \omega_x z')\frac{\partial V''}{\partial y'} + (W'' - \omega_x y')\frac{\partial V''}{\partial z'} = -\frac{\partial \hat{p}}{\partial y'} + \frac{1}{Re}\frac{\partial^2 V''}{\partial x_j' \partial x_j'} - \frac{\partial}{\partial x_j'}\overline{vu_j} + \omega_x W'' \tag{7}$$

$$\frac{\partial W''}{\partial t} + U''\frac{\partial W''}{\partial x'} + (V'' + \omega_x z')\frac{\partial W''}{\partial y'} + (W'' - \omega_x y')\frac{\partial W''}{\partial z'} = -\frac{\partial \hat{p}}{\partial z'} + \frac{1}{Re}\frac{\partial^2 W''}{\partial x_j' \partial x_j'} - \frac{\partial}{\partial x_j'}\overline{wu_j} - \omega_x V'' \tag{8}$$

As a result, all of the centripetal and half the Coriolis terms have been effectively moved to the LHS of (6)-(8) in the form of modified convective velocities. By dropping prime and double prime in the equations, these governing equations have the same form of

the original governing equations in the equation (1) and (2) except for a few terms. The following section uses equations (1) and (2) for other formulation because these additional terms can be simply added in computational coding.

2.2 Turbulence models

A linear eddy viscosity model is used in the current study, where the Reynolds stresses are directly related to the mean rate-of-strain through an isotropic eddy viscosity ν_t. In the Cartesian coordinates,

$$-\overline{u_i u_j} = \nu_t \left(\frac{\partial U_i}{\partial x_j} + \frac{\partial U_j}{\partial x_i} \right) + \frac{2}{3}\delta_{ij} k \tag{9}$$

where δ_{ij} is the Kronecker delta and k is the turbulent kinetic energy.

Substituting (9) for the Reynolds-stress term in (2), the momentum equations in Cartesian coordinates become

$$\frac{\partial U_i}{\partial t} + U_j \frac{\partial U_i}{\partial x_j} = -\frac{\partial P}{\partial x_i} + \frac{1}{R_{U_i}} \frac{\partial^2 U_i}{\partial x_j \partial x_j} + \frac{\partial \nu_t}{\partial x_j} \left(\frac{\partial U_i}{\partial x_j} + \frac{\partial U_j}{\partial x_i} \right) \tag{10}$$

where

$$P = \hat{p} + \frac{2}{3}k \tag{11}$$

$$\frac{1}{R_{U_i}} = \frac{1}{Re} + \nu_t \tag{12}$$

The current study uses the blended *k-w/k-ε* (BKW) turbulence model (Menter, 1993). The idea behind BKW model is to retain the robust and accurate formulation of the *k-ω* model (Wilcox, 1988) in the near wall region, and to take the advantage of the freestream turbulence independency of *k-ε* models (Johns and Launder, 1973) in the outer part of boundary layer. The governing equations for the eddy viscosity ν_t, the turbulent kinetic energy k, and the turbulent specific dissipation rate ω are as follows,

$$\frac{\partial k}{\partial t} + \left(U_j - \sigma_k \frac{\partial \nu_t}{\partial x_j} \right) \frac{\partial k}{\partial x_j} - \frac{1}{R_k} \nabla^2 k + s_k = 0 \tag{13}$$

$$\frac{\partial \omega}{\partial t} + \left(U_j - \sigma_\omega \frac{\partial \nu_t}{\partial x_j} \right) \frac{\partial \omega}{\partial x_j} - \frac{1}{R_\omega} \nabla^2 \omega + s_\omega = 0 \tag{14}$$

$$\nu_t = \frac{k}{\omega} \tag{15}$$

where the source terms, effective Reynolds numbers, and turbulence production are defined as follows

$$s_k = R_k \left(-G + \beta^* \omega k \right) \tag{16}$$

$$s_\omega = R_\omega\left[-\gamma\frac{\omega}{k}G + \beta\omega^2 + 2(1-F_1)\sigma_{\omega 2}\frac{1}{\omega}\frac{\partial k}{\partial x_j}\frac{\partial \omega}{\partial x_j}\right] \tag{17}$$

$$R_k = \left(\frac{1}{1/\mathrm{Re} + \sigma_k \nu_t}\right) \tag{18}$$

$$R_\omega = \left(\frac{1}{1/\mathrm{Re} + \sigma_\omega \nu_t}\right) \tag{19}$$

$$G = \tau_{ij}\frac{\partial U_i}{\partial x_j} = \nu_t\left[\left(U_y + V_x\right)^2 + \left(U_z + W_x\right)^2 + \left(V_z + W_y\right)^2 + 2U_x^2 + 2V_y^2 + 2W_z^2\right] \tag{20}$$

$$F_1 = \tanh\left(\left\{\min\left[\max\left(\frac{\sqrt{k}}{0.09\omega\delta}; \frac{500}{\mathrm{Re}\,\delta^2\omega}\right); \frac{4\sigma_{\omega 2}k}{CD_{k\omega}\delta^2}\right]\right\}^4\right) \tag{21}$$

$$CD_{k\omega} = \max\left(2\sigma_{\omega 2}\frac{1}{\omega}\frac{\partial k}{\partial x_j}\frac{\partial \omega}{\partial x_j}; 10^{-20}\right) \tag{22}$$

The blending function F_1 was designed to be 1 in the sublayer and logarithmic regions of boundary layers and gradually switch to zero in the wake region to take advantage of the strengths of the k-ω and k-ε models, i.e., k-ω does not require near-wall damping functions and uses simple Dirichlet boundary conditions and the k-ε does not exhibit sensitivity to the level of free-stream turbulence as does the k-ω model. The distance to the nearest no-slip surface δ is required for the calculation of F_1 and the model constants are calculated locally as a weighted average, i.e., $\phi = F_1\phi_1 + (1-F_1)\phi_2$ where ϕ_1 are the standard k-ω model and ϕ_2 are the transformed k-ε model constants in Table 1.

Table 1: Blended k-ω/k-ε model constants.

ϕ	ϕ_1	ϕ_2
σ_k	0.5	1.0
σ_ω	0.5	0.856
β	0.075	0.0828
β^*	0.09	0.09
κ	0.41	0.41
γ	0.0553	0.04403

2.3 Equations in generalized curvilinear coordinate

To employ a body-fitted generalized curvilinear coordinate system, the governing equations are transformed from the physical domain in the Cartesian (x, y, z, t) coordinates into the computational domain in non-orthogonal curvilinear coordinates (ξ, η, ζ, τ). A partial transformation is used in which only the independent variables (x, y, z, t) are transformed, leaving the velocity components U_i in the original Cartesian coordinates. The transformation relations are as follows

$$\nabla \cdot \boldsymbol{q} = \frac{1}{J}\frac{\partial}{\partial \xi^j}\left(b_i^j q_i\right) \tag{23}$$

$$\left(\nabla \phi\right)_i = \frac{1}{J} b_i^j \frac{\partial \phi}{\partial \xi^j} \tag{24}$$

$$\nabla^2 \phi = \frac{1}{J}\frac{\partial}{\partial \xi^i}\left(J g^{ij}\frac{\partial \phi}{\partial \xi^j}\right) = g^{ij}\frac{\partial^2 \phi}{\partial \xi^i \partial \xi^j} + f^i \frac{\partial \phi}{\partial \xi^i} \tag{25}$$

$$\frac{\partial \phi}{\partial t} = \frac{\partial \phi}{\partial \tau} - \frac{1}{J} b_i^j \frac{\partial x_i}{\partial t}\frac{\partial \phi}{\partial \xi^j} \tag{26}$$

where q_i represents the components of an arbitrary vector $\boldsymbol{q}(x_i)$. The geometric coefficients b_i^j and g^{ij}, the Jacobian J, and f^i are functions of coordinates only and are defined for Cartesian grids as

$$b_l^i = \varepsilon_{lmn}\frac{\partial x^m}{\partial \xi^j}\frac{\partial x^n}{\partial \xi^k} \quad (ijk \text{ cyclic}) \tag{27}$$

$$g^{ij} = \frac{1}{J^2} b_l^i b_l^j \tag{28}$$

$$J = \begin{vmatrix} x_\xi & x_\eta & x_\zeta \\ y_\xi & y_\eta & y_\zeta \\ z_\xi & z_\eta & z_\zeta \end{vmatrix} \tag{29}$$

$$f^i = \frac{1}{J}\frac{\partial}{\partial \xi^j}\left(J g^{ij}\right) \tag{30}$$

where ε_{lmn} is the permutation symbol. The grid-velocity terms in (26) are used for non-inertial accelerations due to body motions (same as the additional convective terms mentioned previously).

Using the transformation relations, the continuity (1) and momentum equation (10) are written as

$$\frac{1}{J}\frac{\partial}{\partial \xi^i}\left(b_i^j U_j\right) = 0 \tag{31}$$

$$\begin{aligned} \frac{\partial U_i}{\partial \tau} + a_{U_i}^k \frac{\partial U_i}{\partial \xi^k} = &-\frac{1}{J} b_i^k \frac{\partial P}{\partial \xi^k} + \frac{1}{R_{eff}} g^{km}\frac{\partial^2 U_i}{\partial \xi^k \partial \xi^m} \\ &+ \left(\frac{1}{J} b_j^k \frac{\partial \nu_t}{\partial \xi^k}\right)\left(\frac{1}{J} b_i^m \frac{\partial U_j}{\partial \xi^m}\right) \end{aligned} \tag{32}$$

where

$$a_{U_i}^k = \frac{1}{J} b_j^k \left(U_j - \frac{1}{J} b_j^m \frac{\partial \nu_t}{\partial \xi^m} - \frac{\partial x^i}{\partial \tau}\right) - \frac{f^k}{R_{eff}} \tag{33}$$

2.4 Numerical discretization

For temporal discretization, the first-order Euler backward difference is used. For spatial discretization, the convective terms are discretized with the 2nd order upwind difference. The viscous terms are discretized with the 2nd order central difference.

Applying the temporal and spatial discretizations to the momentum equations (32) gives the discretized momentum equations as follows

$$A_{ijk}U_i^n + \sum_{nb} A_{nb}U_{i,nb}^n = S_{U_i} - \frac{1}{J} b_i^k \frac{\partial P^n}{\partial \xi^k} \tag{34}$$

where A_{ijk} and A_{nb} denote the central and neighboring coefficients of the discretized momentum equations, respectively. The source term S_{U_i} contains (*n-1*) velocities and the mixed derivative terms.

2.5 Solution algorithm and pressure poisson equation

The pressure implicit split operator (PISO) algorithm for solving the incompressible Navier-Stokes equations (Issa, 1986) uses a predictor-corrector approach to advance the momentum equation while enforcing the continuity equation. In the predictor step, the algebraic momentum equation (34) is advanced implicitly using the pressure field from the previous time step P^{n-1}

$$A_{ijk}U_i^* + \sum_{nb} A_{nb}U_{i,nb}^* = S_i - \frac{1}{J} b_i^k \frac{\partial P^{n-1}}{\partial \xi^k} \tag{35}$$

where superscript '*' is used to denote advancement to an intermediate time level.

In the corrector step, the velocity is updated explicitly

$$U_i^{**} = \hat{U}_i - \frac{1}{JA_{ijk}} b_i^k \frac{\partial P^*}{\partial \xi^k} \tag{36}$$

using a pressure obtained from a derived Poisson equation and where the psuedo-velocity is defined as

$$\hat{U}_i = \frac{1}{A_{ijk}} \left(S_i - \sum_{nb} A_{nb}U_{i,nb}^* \right) \tag{37}$$

A pressure-Poisson equation is derived by taking the divergence of equation (36) and realizing that the continuity equation (31)

$$\frac{\partial}{\partial \xi^j} \left(\frac{Jg^{jk}}{A_{ijk}} \frac{\partial P^*}{\partial \xi^k} \right) = \frac{\partial}{\partial \xi^j} b_i^j \hat{U}_i \tag{38}$$

Because a regular, or collocated, grid approach is used, solution of equation (38) requires special treatment to avoid even-odd decoupling. The 4th order artificial dissipation

is implicitly added by taking a linear combination of full- and half-cell operators (Sotiropoulos and Abdallah, 1992)

$$(1-\gamma)LP^* + \gamma\hat{L}P^* + NP^* = \frac{\partial}{\partial\xi^j} b_i^j \hat{U}_i \tag{39}$$

where L is the full-cell formulation, $\hat{L}$ is the half-cell formulation, and N is the operator containing mixed-derivative terms

$$L = \delta_{\xi_1}\left(a^{11}\delta_{\xi_1}\right) + \delta_{\xi_2}\left(a^{22}\delta_{\xi_2}\right) + \delta_{\xi_3}\left(a^{33}\delta_{\xi_3}\right) \tag{40}$$

$$\tilde{L} = \tilde{\delta}_{\xi_1}\left(a^{11}\tilde{\delta}_{\xi_1}\right) + \tilde{\delta}_{\xi_2}\left(a^{22}\tilde{\delta}_{\xi_2}\right) + \tilde{\delta}_{\xi_3}\left(a^{33}\tilde{\delta}_{\xi_3}\right) \tag{41}$$

$$N = \delta_{\xi_1}\left(a^{12}\delta_{\xi_2} + a^{13}\delta_{\xi_3}\right) + \delta_{\xi_2}\left(a^{21}\delta_{\xi_1} + a^{23}\delta_{\xi_3}\right) + \delta_{\xi_3}\left(a^{31}\delta_{\xi_1} + a^{32}\delta_{\xi_2}\right) \tag{42}$$

and where

$$\delta_{\xi_i}\phi = \frac{1}{2}\left(\phi_{i+1} - \phi_{i-1}\right) \tag{43}$$

$$\tilde{\delta}_{\xi_i}\phi = \left(\phi_{i+1/2} - \phi_{i-1/2}\right) \tag{44}$$

$$a^{ij} = \frac{Jg^{ij}}{A_{ijk}} \tag{45}$$

The weighting function γ ranges from 1 (i.e., most dissipation and smooth solutions) to 0 (i.e., no dissipation, but prone to decoupling).

The overall method is fully implicit and there are four locations in the code that require iterative solvers: momentum predictor step (34); pressure equation (39); turbulence model equations (13) and (14) for k and ω. Currently, a line-ADI scheme with penta-diagonal solvers and under relaxation is used to solve the algebraic equations. For a given time step, the overall solution method is summarized as follows:

1. Calculate transformation relations, (27)~(30).
2. Solve the discretized two-equation turbulence model equations and calculate eddy viscosity (13), (14) and (15).
3. Solve momentum equations (35).
4. Corrector step, repeat twice.
5. Solve pressure equation (39).
6. Correct velocity field using equation (36).
7. Post-processing.
8. Next time step.

2.6 Chimera overset gridding

Capability for simulations using Chimera-style overset domain decomposition is accomplished through interface with PEGASUS version 5.1i (Suhs et al, 2002), which is the latest version of the PEGASUS series of mesh interpolation codes, developed at NASA Ames Research Center. The main purpose for the development of version 5.1 was to

decrease the number of user inputs required and to allow for easier operation of the code. A basic description of Chimera methodology is described in the Version 4 manual (Suhs and Tramel, 1991).

CFDSHIP-IOWA is designed to use double-fringe hole and outer boundaries and level-2 interpolation. The double-fringe permits use of the normal 5-point stencil for all field points and maintains order of accuracy near boundaries as 2nd order. The downside in using a double fringe is that it requires more mesh points and makes it more difficult to obtain the required overlap between hole boundaries and outer boundaries. The level-2 interpolation provides capability to create holes with refinement meshes that are added to the domain. This cannot be accomplished through the usual hole-cutting methods, since refinement meshes typically do not have solid walls that would be used for definition of hole-cutting boundaries.

2.7 Parallel computing

CFDSHIP-IOWA achieves scalable parallel performance using several parallel models. Originally, it was designed as a distributed-memory coarse-grain message-passing model based upon domain decomposition and the message-passing interface (MPI). For good performance, this approach requires static load balancing, i.e., the grid system be decomposed into nearly equal sized blocks, and, in addition, requires a block for each processor. While very efficient, this process becomes tedious and makes post-processing difficult, especially when large numbers of processors (>32) are required. To alleviate this problem, a second parallel model using OpenMP threads for shared-memory fine-grain parallelism was introduced. This model is used in combination with MPI to achieve multi-level parallelism, which permits use of very large number of processors and can perform dynamic load balancing.

3 Ducted marine propulsor 5206 and EFD validation data

The model propeller P5206 is a three bladed rotor in a cylindrical duct. All experimental measurements were made in the 36-inch water tunnel at the Naval Surface Warfare Center, Carderock Division (NSWCCD). The tunnel is a recirculating design with interchangeable test sections. The 36-inch diameter, open jet test section was used for these tests. Figure 1 shows a schematic experimental setup of ducted rotor at the 36-inch water tunnel. This configuration produces an inner duct diameter of 0.8636 m (34 inches), the largest propeller operated in the 36-inch water tunnel.

The measured flow conditions are given on Table 2. The operating advance coefficient J was selected to produce a typical tip-leakage vortex. Laser Doppler Velocimetry (LDV) were taken upstream and downstream of the rotor and circumferentially averaged flow data was provided at upstream x/D =-0.179, and downstream x/D =0.37 of the rotor, shown in Figure 1, where x = 0 corresponds to the center of the 12-inch long propeller hub. LDV measurements were made intensively along the tip-leakage vortex at 103 different x-r planes, which cover up to S = 1.6. The planes for comparison are selected at S = 1.02, 1.1, 1.2, 1.3, 1.4 and 1.5, defined as

$$S = \frac{R\theta}{C} + 1 \tag{46}$$

where R is the radius of rotor and C is the chord length at the blade tip. $S = 1$ indicates the trailing edge of blade tip. Figure 2 shows the schematic view of these planes.

Table 2: Measured flow conditions

N	J	U_o (m/s)	K_T	K_Q	Re
500	0.983	6.965	0.31	0.056	6×10^6

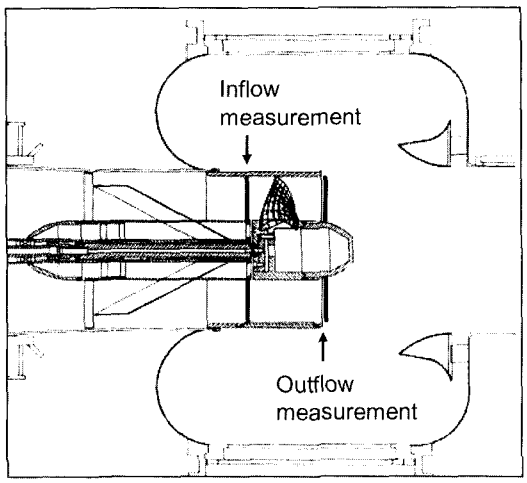

Figure 1: The schematic view of the experiments

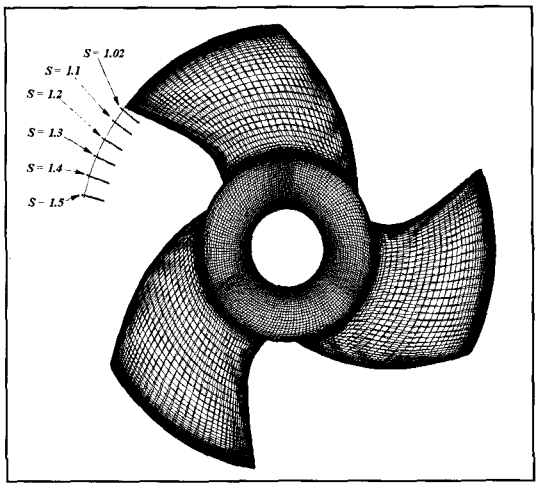

Figure 2: Comparison planes in S coordinate

4 Verification and validation (V&V)

Verification & Validation (V&V) approach of Stern et al (2001) is followed. Three systematically refined grids are required. Non-integer grid refinement ratio $r_G = \sqrt{2}$ is selected in the current study. The fine grid is generated at first. Removing every second point in the fine grid can generate the coarse grid, but due to the non-integer refinement ratio, the medium grid is generated by an interpolation method.

The difficulty to construct the structured grid system on ducted marine propulsor is due to high pitch angle of the blade and tip-gap between the blade tip and the duct. The conventional H-type grid, which passes through the passage of pressure side and suction side of the propeller and is mostly used in RANS simulation of open water propellers, has a limitation to make high-resolution grid in the region of tip-gap and expected leakage vortex area. In order to avoid above problems, Chimera overset grid method is adopted to achieve high resolution for the tip-gap and the leakage-vortex area. The whole grid system is composed of three structured grid blocks such as blade, tunnel passage and refined grids on leakage vortex area. The tunnel grid block consists of six divided blocks and the blade and refined grid block consist of four and three divided blocks respectively. Therefore the whole grid system consists of patched and overlapping multi-block grids shown in Figure 3. The numbers of grid points for coarse, medium, and fine are 261,936 points, 933,495 points and 2,053,982 points respectively.

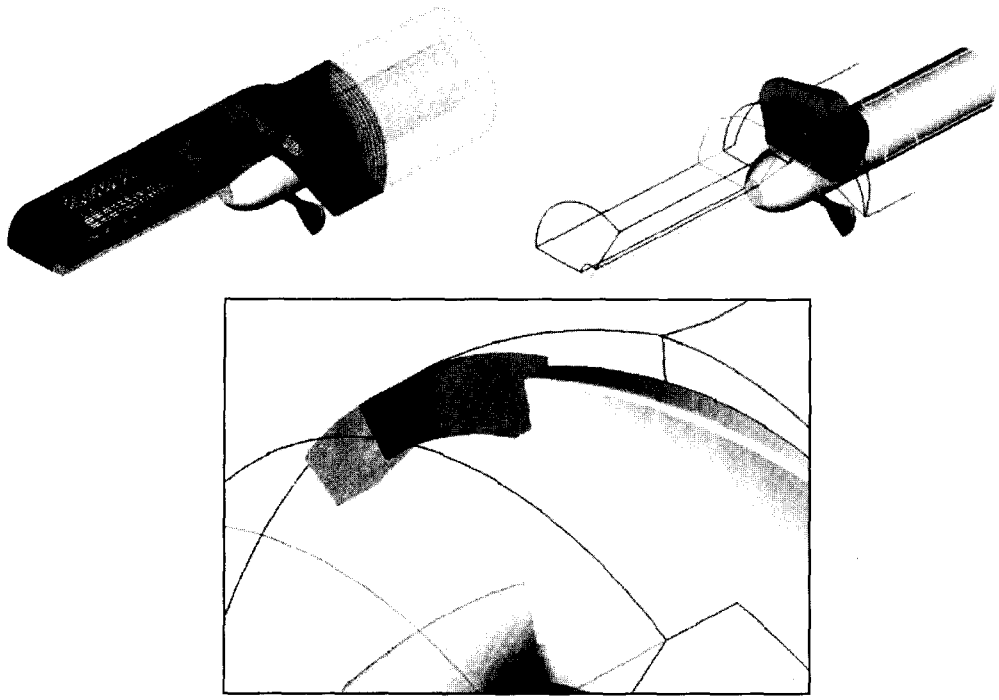

Figure 3: The used grid system

The following boundary conditions are used as shown in Figure 4: the inlet plane S_I; the exit plane S_E; the polar periodic plane S_{PP}; the axis pole boundary S_P; the no-slip plane S_{NS}; the rotating no-slip plane S_{RNS}; the multi-block interface plane S_{MB}.

On the inlet plane S_I, the actual tunnel flow is not fully developed so that the boundary layer of the tunnel wall is increasing after the contraction part of the water tunnel. In order to match the measured thickness of the boundary layer at x/D=-0.179, the position of the inlet plane is adjusted at x/D=-1.49, which is achieved through several simulations of tunnel block grids. The center point of this plane is used for the reference pressure by setting its value to zero. On the exit plane S_E, internal flow usually needs special treatment of the boundary conditions to ensure mass conservation. The flux difference between the inlet and exit plane is corrected at the exit plane. This treatment improves the convergence of the global solution. On the polar periodic plane S_{PP}, since the Cartesian coordinate system is used, V and W velocity components are converted to the cylindrical coordinate velocity component, V_r and V_θ, in order to apply the polar periodic boundary condition. On the axis pole boundary S_P, this boundary covers the singular line along the x-axis after the fairwater up to the exit plane shown. On the no-slip plane S_{NS}, NSWCCD 36-inch water tunnel is open jet type, but it is simplified as closed circular tunnel. So, the duct is extended downstream with constant radius. The no-slip boundary covers the tunnel wall, fairwater, and propeller shaft except for the rotating hub. On the rotating no-slip plane S_{RNS}, the rotating no-slip boundary condition is applied to blade surface and rotating part of propeller hub. On the multi-block interface plane S_{MB}, the linear interpolation is used for the values of physical variables. The boundaries related with grid overlapping are interpolated or blanked out after the successful run of PEGASUS.

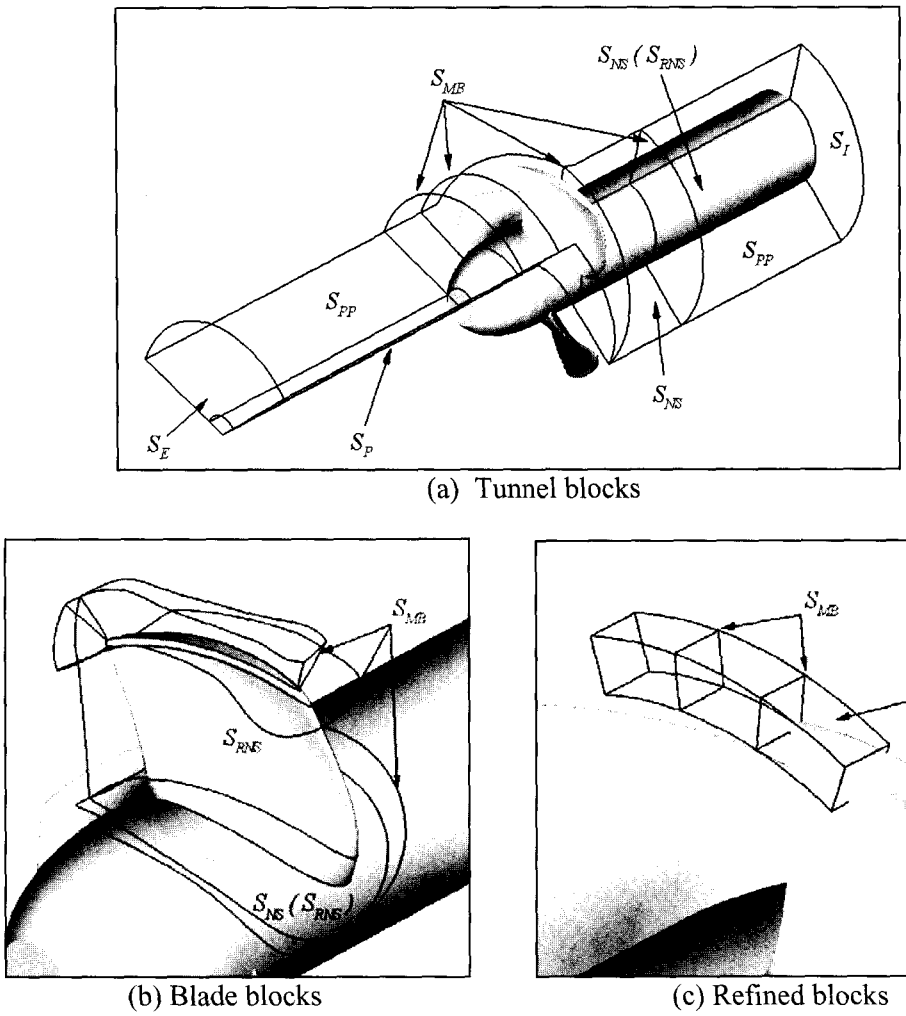

(a) Tunnel blocks

(b) Blade blocks

(c) Refined blocks

Figure 4: Schematic view of boundary conditions for the ducted marine propulsor P5206

Both integral and point variables are used for V&V analysis. Each solution for all three grids shows iterative convergence by displaying about 3 orders of magnitude drop in the pressure residuals and 4 orders of magnitude drop in velocities and turbulence model quantities. An example is shown in Figure 5, which displays the residuals for the fine grid solution. Since iterative convergence is obtained, it is possible to estimate the iterative uncertainty. The iterative history of thrust and torque coefficients are shown in Figure 6 and 7. The oscillatory iterative convergence is achieved in both K_T and K_Q values for all three grids. The iterative uncertainty, U_I can be estimated from last five hundred iterations in the iterative history based on the range of the maximum and minimum values.

For K_T, the iterative uncertainty U_I for the fine grid is found to be $0.32\% S_1$, where S_1 implies the converging K_T value for the iterative history of the fine grid. For K_Q, $0.13\% S_1$ for the fine grid is obtained. The iteration errors and uncertainties are small in comparison to grid errors and uncertainties (grid errors and uncertainties are assessed as following). By neglecting the iterative uncertainty, we have the simulation numerical uncertainty U_{SN} equal to the grid uncertainty U_G.

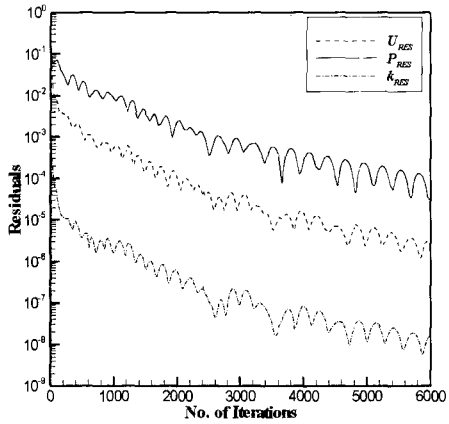

Figure 5: The residuals of axial velocity, pressure and turbulent kinetic energy

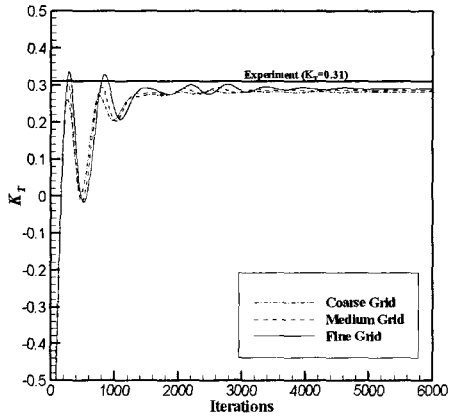

Figure 6: The iterative history of thrust coefficients

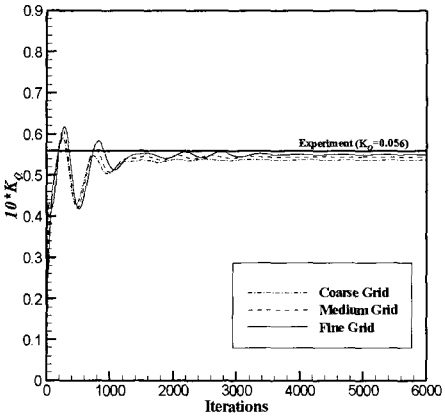

Figure 7: The iterative history of torque coefficients

4.1 Verification & validation of integral variables

The thrust and torque are used for the integral variables in V&V procedure. Table 3 shows the grid convergence for the thrust coefficient (K_T) and the torque coefficients (K_Q). It also shows the change in solution. With the two solution changes known, it is possible to calculate the grid convergence ratio. This will give information about the convergence condition.

Table 3: The grid convergence of integral variables

	Coarse (S_3)	Medium (S_2)	Fine (S_1)	Data (D)
K_T	0.2830	0.2870	0.2895	0.31
	8.7%	7.4%	6.6%	
ε		-0.0040	-0.0025	
K_Q	0.05385	0.05460	0.05498	0.056
	3.8%	2.5%	1.8%	
ε		-0.00075	-0.00038	

The current study displayed monotonic convergence. The simulation numerical uncertainty U_{SN} , validation uncertainty $U_V = \sqrt{U_D^2 + U_{SN}^2}$, comparison error E=D-S, and estimated U_D are shown in Table 4. For K_T, $|E| > U_V$ such that K_T is not validated at the $|E| = 6.6\%D$. For K_Q, $|E| < U_V$, such that K_Q is validated at $|U_V| = 2.3\%D$. Present V&V intervals seem reasonable in comparison previous results with CFDSHIP-IOWA for open water propeller (Chen, 2000), i.e., E=2.4%D for K_T and 3.8%D for K_Q and surface combatant and Brewer (2002) results for same ducted propulsor, i.e., E=19%D for K_T and 0%D for K_Q.

Table 4: Validation of integral variables

	E (%D)	U_V (%D)	U_D (%D)	U_{SN} (%D)
K_T	6.6	3.3	2.2	2.4
K_Q	1.8	2.3	2.2	0.74

4.2 Verification and validation of a point variable

The radial velocity V_r along the horizontal-cut line from 0.07 < x/D < 0.12 at r/D = 0.494 in the plane S = 1.02 shown in Figure 13 is selected as a point variable. This horizontal-cut line passes through the center of tip-leakage vortex core in the axial direction. The plane S = 1.02 corresponds to the plane just after the trailing edge of the blade shown in Figure 2. The grid convergence for the radial velocity along the horizontal-cut is shown in Figure 8, including comparison with experimental data. The simulation results do capture the gradient or magnitude of the tip-leakage vortex. A second peak is also observed in the data, which as will be discussed later corresponds to the training edge vortex.

The profile-averaged validation results for the radial velocity profile are given in Table 5. Values are normalized with the maximum value for the radial velocity profile in data ($V_{r\max} = 1.5$). The data uncertainty for LDV measurement in mean velocity is 2 – 5 % of maximum velocity (Longo, 2002) and so it is assumed $U_D = 3.7\%V_{r\max}$. $|E| < U_V$ such that the solution is validated globally at $|U_V| = 4.5\%V_{r\max}$ level.

In Chen(2000)'s V&V analysis, he also used the velocity profile of the tip vortex as the point variable. He obtained the profile-averaged error E=5.1% and validation uncertainty U_V=6.5%. The current result shows a little smaller error and validation uncertainty than Chen's.

Distributions of $(E, \pm U_V)$ along the horizontal-cut line are also computed and showed in Figure 9. The lack of validation is mainly due to under prediction of radial velocity gradient and magnitude near vortex core in the simulation.

Table 5: The profile-averaged validation of a point variable

E $\%V_{r\max}$	U_V $\%V_{r\max}$	U_D $\%V_{r\max}$	U_{SN} $\%V_{r\max}$
3.9	4.5	3.7	2.6

($V_{r\max} = 1.5$)

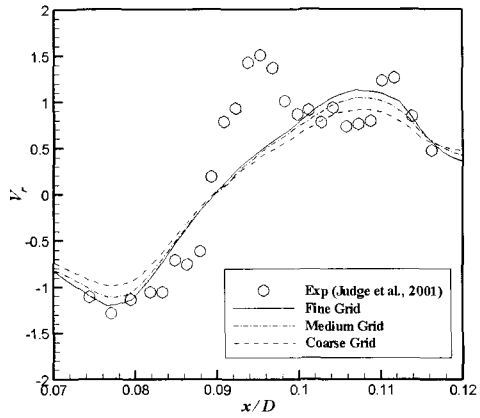

Figure 8: The grid convergence of radial velocity profile along the horizontal-cut line

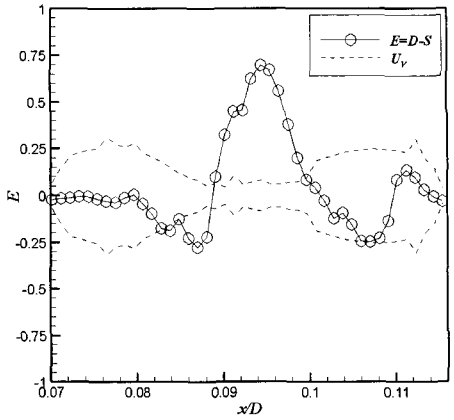

Figure 9: The error and validation uncertainty

5 Analysis of propulsor flow and tip-leakage vortex

The propulsor flow is very sensitive to the inflow coming into the propulsor blade rows. Especially, the boundary layer thickness affects significantly the performance of propulsor such as thrust and torque. Additional effort is needed to calibrate the inflow such that the numerical simulation represents the experimental flow conditions. Calibration is performed by systematically adjusting the inlet position in order to get the same boundary layer thickness at the measured inflow condition, x/D = -0.179 shown in Figure 1. In Figure 10, circumferentially averaged velocity profiles from the RANS solution are compared with experimental measurements. The axial velocity profile is nicely matched with experimental measurements.

Comparisons of circumferentially averaged velocities in outflow are made with experimental measurements. Figure 11 shows the circumferentially averaged axial velocity profile including the experimental data measured at x/D = 0.37. This position corresponds to the axial location just after the duct trailing edge. The computed profiles are in overall good agreement with the experimental data. The simulated axial velocity shows a little bigger acceleration near hub region. The discrepancy near the duct region is due to the existence of the duct wall in the simulation modeling. On the contrary, the experimental flow is an open jet after the duct trailing edge.

Figure 12 shows the pressure distribution on the surface of the blade and hub. The denoted P in this figure is non-dimensionalized by ρU_o^2, and so it can be converted to C_P by multiplying by 2. The minimum pressure on the blade surface is obtained on the suction side of blade tip at 84% of the tip chord length (S = 0.84) with a value P = -4.4. Typically cavitation inception number $\sigma_i = -C_{P\min}$ is used as a rough estimate of the cavitation inception. The current results give the cavitation inception number $\sigma_i = 8.8$. However, cavitation inception bubble is experimentally observed to occur at the downstream of half tip chord length (S = 1.5) along tip-leakage vortex with the value of cavitation inception number $\sigma_i = 11$. Figure 13 shows the pressure distribution of the duct surface. The pressure variation of the blade tip and the tip-leakage vortex are significantly felt on the duct surface. Low pressure along the tip-leakage vortex is clearly shown.

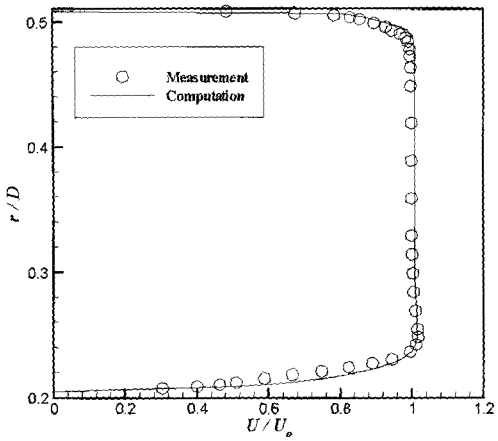

Figure 10: Comparisons of axial velocity profile at $x/D = -0.179$

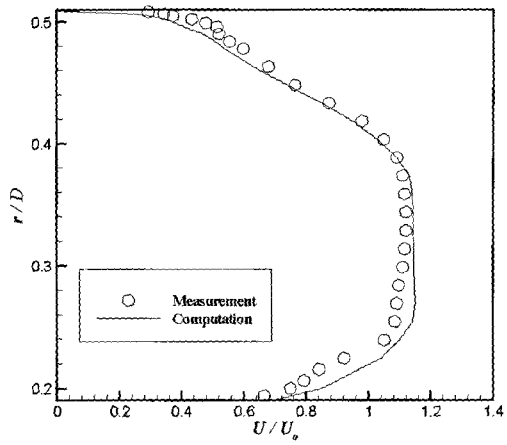

Figure 11: Comparisons of axial velocity profile at $x/D = 0.37$

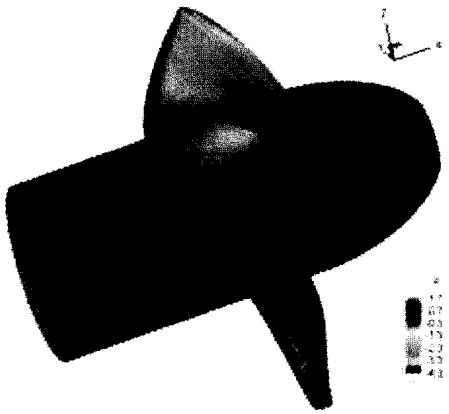

Figure 12: Pressure on the surface of blade and hub

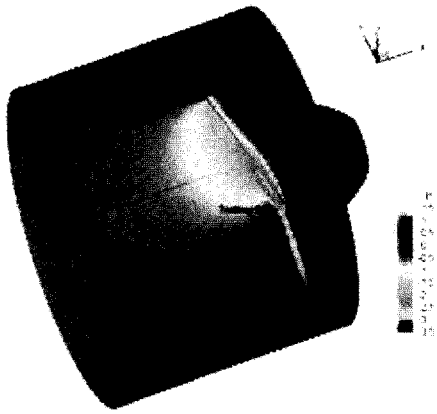

Figure 13: Pressure on the duct surface

In order to capture the flow structure of the tip-leakage vortex, a ribbon tracing is performed along the tip-leakage vortex and trailing edge vortex. Figure 14 shows how the co-rotating tip-leakage and trailing edge vortices interact (S=1.02) and merge S>1.02 with low pressure, especially along the tip-leakage vortex core.

Cross flow velocity vectors (U,V_r) in x-r plane and contours of tangential velocity in rotor rotation direction V_T are compared. The streamlines are traced to capture the shape of vortex and vortex core center. At the plane S = 1.02 corresponds just downstream of the rotor tip, both results show the blade wake and the interaction between the tip-leakage and the trailing edge vortices in Figure 15. The computational result does not show clearly the vortical vector near the tip trailing edge (the trailing edge vortex will be shown clearly by vorticity contour in the following). The overall shape of vortex is distorted by the effect of the interaction of the two vortices. Streamlines in the computation are more diffusive than experiment. Both results show faster vortex core velocity in the contours of V_T than the surroundings. The position of the vortex core is well matched with the experiment.

The axial vorticity is computed with both computational and experimental results. At the plane $S = 1.02$ (Figure 16), the existence of trailing edge vortex is clearly shown in the computational result, which was not shown with the cross plane vectors in Figure 13. The experiment shows that two peak values at the center of each vortex core and another peak value between the tip-leakage vortex and the trailing edge vortex. RANS computation only shows a peak value of vorticity at the center of the trailing edge vortex. The peak value between the tip-leakage vortex and the tailing edge vortex in the experiment seems to be related to the vortex interaction. RANS solution does not catch the vortex interaction accurately in this plane.

After the plane of vortex interaction ($S > 1.02$), two vortices are merged along the tip-leakage vortex near S=1.1. The vortex strength is temporally increasing just after merging and decreasing after that. The detail comparisons at other S-planes are not shown in the current paper, but it can be found in the thesis paper (Kim, 2002) including comparisons of the vortical velocity profiles at the vertical and horizontal cut lines shown in Figure 13.

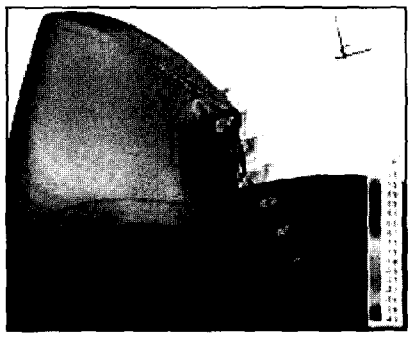

Figure 14: Flow Structures in the tip-leakage vortex area

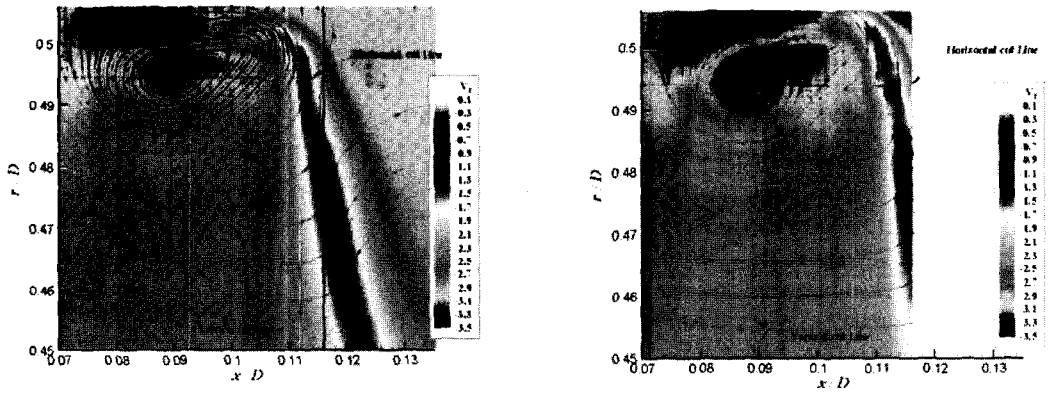

(a) Computation (b) Experiment

Figure 15: Cross plane velocity vectors and tangential velocity contour at $S = 1.02$

The position of the vortex core is compared with experimental data and other computational results (Brewer, 2002) in Figure 17. The symbols for the experiment and the current computation indicate each S-plane (1.02 – 1.5) in sequential order. The symbols for Brewer's computation represent the S values of 1.03, 1.07, 1.17 and 1.23 respectively. The computed results show the good agreement except for $S > 1.3$. From $S = 1.3$, the position of the vortex core in the current computation is shifted to the axial flow direction compared

to the experiment. Brewer's(2002) result is overall shifted toward upstream compared to the experiment

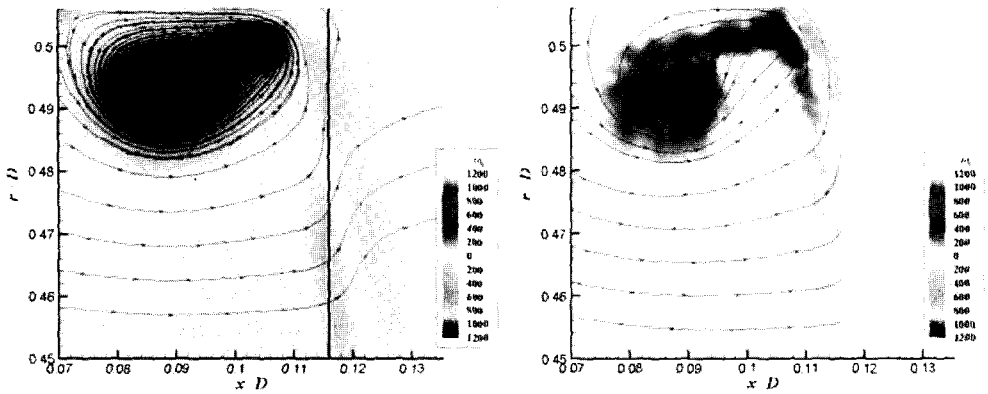

(a) Computation (b) Experiment

Figure 16: Vorticity contours at $S = 1.02$

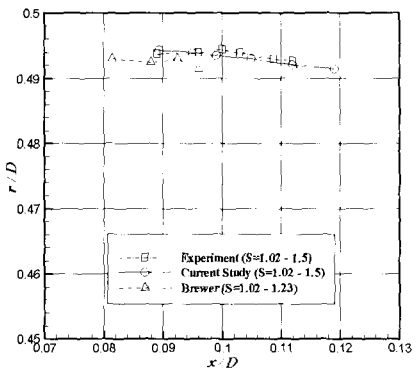

Figure 17: The position of tip-leakage vortex core

In order to compare the global characteristic of the tip-leakage vortex, the vortex core size and the circulation is computed. The vortex shape is not symmetric and so the core size is obtained in an averaged sense. The computed values are shown in Figures 18 and 19. The vortex core size in the computation is bigger than in the experiment and the circulation shows a good agreement with the experiment except at the plane $S = 1.02$, where the vortex interaction occurs.

Figure 20 shows the pressure coefficient C_P along the vortex core computed from the current RANS solution and the computational solution by Brewer (2002). The current study gives much lower level of the pressure coefficient than Brewer's result. The minimum pressure coefficient is obtained at $S = 1.08$ with value C_P = -6.4. This value is higher than the coefficient of blade minimum pressure (C_P = -8.8) and even much higher than experimental cavitation inception number (σ_i=1.1). Therefore, based on the current RANS solution, low pressure in the vortex core region does not affect the cavitation inception based on $\sigma_i = -C_{p\,min} = 6.4$.

Even though the experimental data for the pressure along the tip-leakage vortex is not provided, a rough comparison is possible from the photo of the tip-leakage vortex cavitation taken in the experiment. Figure 21(a) shows the photo taken at 18 *psi* tunnel pressure. The tunnel pressure gives the cavitation number through simple calculation by

the definition of cavitation number. The converted cavitation number is $\sigma = 5.0$. Under the assumption that a region with $C_P < -\sigma$ is cavitating, Figure 21(b) shows the iso-surface of $C_P = -5.0$. Comparison shows very similar cavitating region. The results of the comparison being so positive leads to the conclusion that the pressure distribution in Figure 18 is a good prediction of the distribution within the cavitation zone.

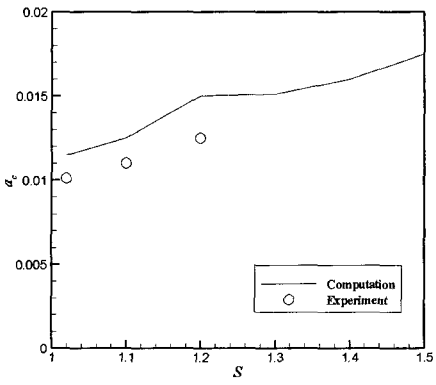

Figure 18: Vortex core size

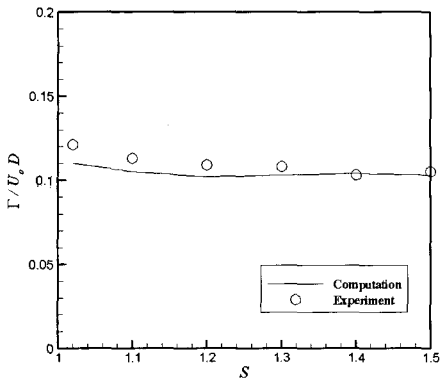

Figure 19: Circulation

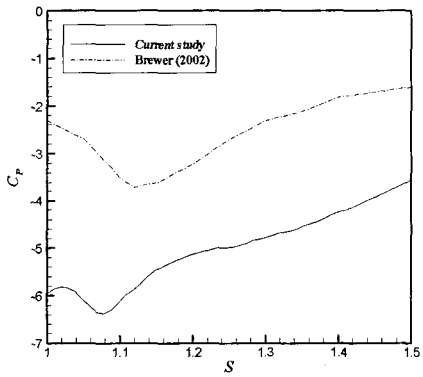

Figure 20: Pressure along the tip-leakage vortex

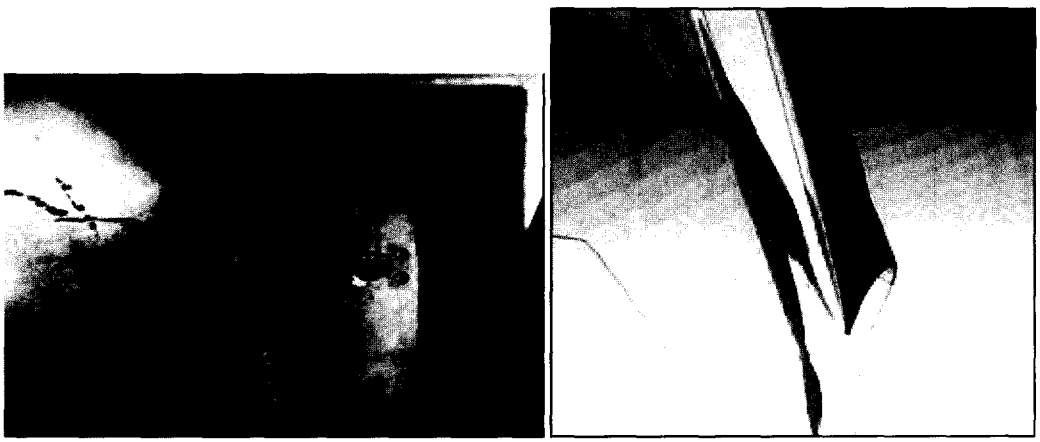

(a) Experiment (b) Computation

Figure 21: Cavitation comparison with experime

6 Summary and conclusions

High-fidelity RANS CFD simulations are presented for the ducted marine propulsor 5206, including verification studies based on assessment iterative and grid convergence, validation studies using available benchmark EFD data. The general-purpose, parallel, unsteady RANS code CFDSHIP-IOWA is used with the blended k-ε/k-ω turbulence model and extensions for the relative rotating coordinate system and Chimera overset grids method. Intervals verification for thrust, torque, and profile averaged radial velocity are 2.4, 0.74, and 2.6%D, which are reasonable in comparison with previous results for open water propellers and surface combatant. Thrust not validated since comparison error E=7%D and validation uncertainty U_V=3%D, but torque validated at 2%D. Just downstream of the rotor tip, the average radial velocity is validated at 5%V_{rmax}, but under prediction magnitude and gradients in vortex cores. Flow pattern displays interaction (just down stream of rotor tip) and merging (after 10% chord length downstream rotor tip) of tip-leakage and trailing edge vortices. In interaction region, multiple peaks and magnitude of vorticity under predicted, whereas in merging region, better agreement although magnitudes in vortex cores still under predicted. Tip-leakage vortex core position, size, and circulation show good agreement data, although size over predicted and circulation in interaction region under predicted. For cavitation number σ=5 and assuming $C_P < -5$ as the cavitation condition for the simulations, EFD and CFD cavitation patterns show good agreement. The simulations indicate globally minimum $C_P = -\sigma_i = -8.8$ on the suction side of the blade tip at 84% of the chord length from leading edge and locally minimum $C_P = -6.4$ in the tip-leakage vortex at 8% chord downstream trailing edge, which implies cavitation inception number $\sigma_i = 8.8$ and location on the blade near tip trailing edge. EFD indicated $\sigma_i = 11$ and location in tip-leakage vortex core 50% chord downstream trailing edge. More complex modeling including two-phase bubble dynamic model would be recommended for the study of cavitation inception process.

Acknowledgements

This research was sponsored by Office of Naval Research grant N00014-00-1-0473 under the administration of Dr. Patrick Purtell and partially supported to prepare this paper by the basic research project in KRISO/KORDI.

References

Abdel-Maksoud, M., F. Menter and H. Wuttke. 1998. Viscous flow simulations for conventional and high-skew marine propellers. Ship Technology Research, **45**, 64-71.

Brewer, W.H. 2002. On simulating tip-leakage vortex flow to study the nature of cavitation inception. Ph.D. Thesis, Mississippi State University.

Chen, B. and F. Stern. 1998. Computational fluid dynamics of four-quadrant marine-propulsor flow. ASME Symposium on Advances in Numerical Modeling of Aerodynamics and Hydrodynamics in Turbomachinery.

Chen, B. 2002. RANS simulation of tip vortex flow for a finite-span hydrofoil and a marine propulsor. Ph.D. Thesis, The University of Iowa.

Chizelle, Y.K., S.L. Ceccio and C.E. Brennen. 1995. Observations and scaling of traveling bubble cavitation. J. of Fluid Mechanics, **293**, 99-126.

Feng, J., V.A. Wang, Y.T. Lee and C.L Merkle. 1998. CFD modeling of tip vortex for open marine propeller. ASME FED Summer Meeting.

Hsiao, C.T. and G.L. Chahine. 2001. Numerical simulation of bubble dynamics in a vortex flow using Navier-Stokes computations and moving Chimera grid scheme. CAV2001: The 4th International Symposium on Cavitation.

Hsiao, C.T. and G.L. Chahine. 2002. Prediction of vortex cavitation inception using coupled spherical and non-spherical models and UnRANS computations. The 24th Symposium on Naval Hydrodynamics.

Hsiao, C.T. and L.L. Pauley. 1997. Numerical study of tip vortex cavitation inception using a bubble dynamics model. ASME FED Summer Meeting (FEDSM 97-325).

Hsiao, C.T. and L.L. Pauley. 1998. Numerical computation of tip vortex flow generated by marine propeller. ASME FED Summer Meeting.

Issa, R.I. 1986 Solution of implicitly discretized fluid flow equations by operator splitting. J. of Comput. Phys., **62**, 40-65.

Jones, W.P. and B.E. Launder. 1973. The calculation of low-Reynolds-number phenomena with a two-equation model of turbulence. Int. J. of Heat Mass Transfer, **16**, 1119-1130.

Judge, C.Q., G.F. Oweis, S.L. Ceccio, S.D. Jessup, C.J. Chesnakas and D.J. Fry. 2001. Tip-leakage vortex interaction on a ducted rotor. CAV 2001: The 4th International Symposium on Cavitation.

Kim, J. 2002. Sub-visual cavitation and acoustic modeling for ducted marine propulsor. Ph.D. thesis, The University of Iowa.

Longo, J. Personal Communications.

Menter, F. 1993. Zonal two-equation k-ω turbulence models for aerodynamic flows. AIAA Paper 93-2906.

Paterson, E.G., R.V. Wilson and F. Stern. 2003. General purpose parallel unsteady RANS ship hydrodynamics code: CFDSHIP-IOWA. IIHR Report, **30**, in preparation, The University of Iowa.

Sanchez-Caja, A. 1996. Numerical calculation of viscous flow around DTRC propeller 4119 for advance number range 0.3-1.1 using the FINFLO Navier-Stokes solver. Technical Report VALB141A, VTT Manufacturing Technology, Tekniihantie **12**.

Sotiropoulos, F. and S. Abdahllah. 1992. A primitive variable method for the solution of three-dimensional incompressible viscous flow. J. of Comput. Phys., **103**.

Stern, F., R.V. Wilson, H. Coleman and E.G. Paterson. 2001. Comprehensive approach to verification and validation of CFD simulations – Part 1: Methodology and Procedure. ASME. J. of Fluids Engineering, **123**, **4**, 793-802.

Stern, F., D. Zhang, B. Chen, H. Kim and S. Jessup. 1994. Computation of viscous marine propulsors blade and wake flow. The 21st ONR Symposium on Naval Hydrodynamics.

Suhs, N.E., S.E. Rogers and W.E. Dietz. 2002. PEGASUS 5: An Automated Preprocessors for Overset-Grid CFD. AIAA Paper No. 2002-3186.

Suhs, N. E. and R.W. Tramel. 1991. PEGASUS 4.0 User's Manual, AEDC-TR-91-9

Wilcox, D.C. 1988. Reassessment of the scale-determining equation for advanced turbulence models. AIAA J., **26**, 1299-1310.

Wilson, R.V., E.G. Paterson and F. Stern. 2000. Verification and validation for RANS simulation of a naval combatant. Gothenburg 2000: A Workshop on Numerical Ship Hydrodynamics.

Wilson, R.V., F. Stern, H. Coleman and E.G. Paterson. 2001. Comprehensive approach to verification and validation of CFD simulations – Part 2: Application for RANS simulation of cargo/container ship. ASME J. of Fluids Engineering, **123**, **4**, 803-810.